JMEPEG (2011) 20:1097–1108
DOI: 10.1007/s11665-010-9741-y

1059-9495/$19.00

Computational Investigation of Hardness Evolution During Friction-Stir Welding of AA5083 and AA2139 Aluminum Alloys

M. Grujicic, G. Arakere, C.-F. Yen, and B.A. Cheeseman

(Submitted July 19, 2010)

A fully coupled thermo-mechanical finite-element analysis of the friction-stir welding (FSW) process developed in our previous work is combined with the basic physical metallurgy of two wrought aluminum alloys to predict/assess their FSW behaviors. The two alloys selected are AA5083 (a solid-solution strengthened and strain-hardened/stabilized Al-Mg-Mn alloy) and AA2139 (a precipitation hardened quaternary Al-Cu-Mg-Ag alloy). Both of these alloys are currently being used in military-vehicle hull structural and armor systems. In the case of non-age-hardenable AA5083, the dominant microstructure-evolution processes taking place during FSW are extensive plastic deformation and dynamic re-crystallization of highly deformed material subjected to elevated temperatures approaching the melting temperature. In the case of AA2139, in addition to plastic deformation and dynamic recrystallization, precipitates coarsening, over-aging, dissolution, and re-precipitation had to be also considered. Limited data available in the open literature pertaining to the kinetics of the aforementioned microstructure-evolution processes are used to predict variation in the material hardness throughout the various FSW zones of the two alloys. The computed results are found to be in reasonably good agreement with their experimental counterparts.

Keywords AA2139, AA5083, finite-element analysis, friction-stir welding, hardness prediction

1. Introduction

Having a more mobile, deployable, and sustainable fleet which will maintain or surpass the current levels of its lethality and survivability has become one of the main recent goals of the U.S. Army. Current battlefield vehicles have reached in excess of 70 tons due to ever increasing lethality of ballistic threats which hinders their ability to be readily transported and sustained. Therefore, a number of research and development programs are under way to engineer light-weight, highly mobile, transportable, and lethal battlefield vehicles with a target weight less than 20 tons. To attain these goals, significant advances are needed in the areas of light-weight structural- and armor-materials development (including aluminum-based structural/armor-grade materials).

Aluminum alloy AA5083-H131 has been historically used in military-vehicle systems such as the M1113 and the M109, in accordance with the MIL-DTL-46027J specification (Ref 1). The main reasons for the selection of this alloy are its lighter weight, ease of joining by various welding techniques, a relatively high level of performance against fragmentation-based threats, and superior corrosion resistance. To respond to the advent of more lethal threats, recently designed aluminum-armor-based military-vehicle systems, such as the M2 Bradley Fighting Vehicle, have relied on the use of higher strength aluminum alloys, such as AA2139 (Ref 2), AA7039 (Ref 3), AA2219 (Ref 4), and AA2519 (Ref 5). These alloys provide increased ballistic protection against armor piercing (AP) threats due to their higher strength. In addition, higher tensile strength levels offered by these alloys are very desirable for vehicle-hull designs as they enable significant reductions in the vehicle weight. However, these alloys also show some significant shortcomings primarily due to their lower weldability and inferior corrosion resistance in comparison to that observed in AA5083-H131.

In the present work, a series of computational analyses is carried out in order to assess and compare welding behavior of AA5083-H131 and one of the newer high-strength aluminum alloys AA2139. Since these alloys are often welded using friction-stir welding (FSW), only the FSW joining behavior of these two alloys is investigated in the present work.

In contrast to the traditional fusion-welding technologies, FSW is a solid-state metal-joining process which is generally employed in applications in which the original material microstructure/properties must remain unchanged as much as possible after joining (Ref 6-8). In this process, as shown in Fig. 1(a), a rotating tool moves along the contacting surfaces of two rigidly butt-clamped plates. As seen in this figure, the tool consists of a cylindrical pin which is threaded, at one end, and equipped with a shoulder, at the other. Also, during joining, the work-piece (i.e., the two clamped plates) is generally placed on a rigid backing support. At the same time, the shoulder is forced to make a firm contact with the top surface of the work-piece.

M. Grujicic and **G. Arakere**, Department of Mechanical Engineering, Clemson University, 241 Engineering Innovation Building, Clemson, SC 29634-0921; and **C.-F. Yen** and **B.A. Cheeseman**, Army Research Laboratory, Survivability Materials Branch, Aberdeen, Proving Ground, MD 21005-5069. Contact e-mail: mica.grujicic@ces.clemson.edu.

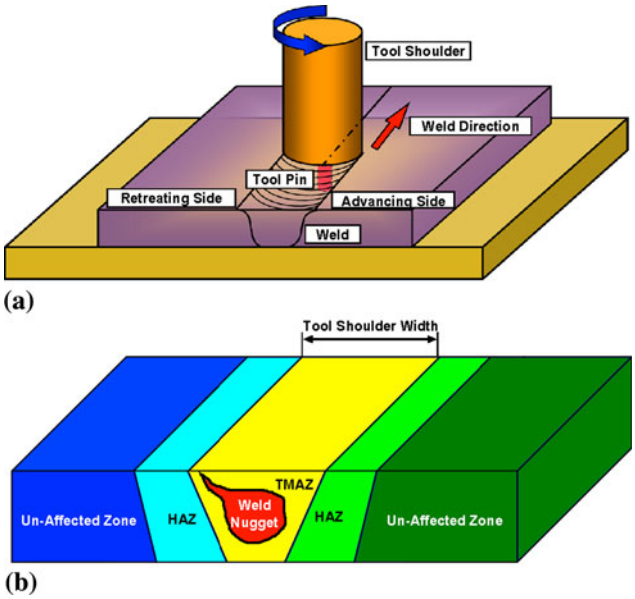

Fig. 1 (a) A schematic of the friction stir welding (FSW) process and (b) the main microstructural zones associated with the typical FSW joint

As the tool (rotates and) moves along the butting surfaces, heat is being generated at the shoulder/work-piece and, to a lesser extent, at the pin/work-piece contact surfaces, as a result of the frictional-energy dissipation. This, in turn, causes an increase in temperature and gives rise to softening of the material adjacent to these contacting surfaces. As the tool advances along the butting surfaces, thermally softened material in front of the tool is (heavily) deformed, extruded around the tool to the region behind the tool and compacted/forged to form a joint/weld.

FSW has become the preferred technique for joining/welding *Difficult-to-weld* metals like aluminum alloys, since its discovery in 1991 (Ref 6). Currently, shipbuilding, marine, aerospace, railway, and land transportation industries use FSW extensively as a joining process. Relative to the traditional fusion-welding technologies, FSW offers a number of advantages such as (a) good mechanical properties in the *as-welded* condition; (b) improved safety due to the absence of toxic fumes or the spatter of molten material; (c) no consumables such as the filler metal or gas shield are required; (d) ease of process automation; (e) ability to operate in all positions (horizontal, vertical, overhead, orbital, etc.), as there is no weld pool; (f) minimal thickness under/over-matching which reduces the need for expensive post-weld machining; and (g) low environmental impact. However, some disadvantages of the FSW process have also been identified such as (a) an exit hole is left after the tool is withdrawn from the work-piece; (b) relatively large tool press-down and plates-clamping forces are required; (c) lower flexibility of the process with respect to variable thickness and non-linear welds; and (d) often associated with lower welding rates than conventional fusion-welding techniques, although this shortcoming is somewhat lessened since fewer welding passes are required.

Various thermo-mechanical processes such as friction-energy dissipation, plastic deformation and the associated heat dissipation, material transport/flow, dynamic recrystallization, local cooling, etc., and their complex interactions play a critical role in the FSW process (Ref 9-19). Metallographic examinations of the FSW joints typically reveal the existence of the following four zones, Fig. 1(b): (a) an un-effected zone which is far enough from the weld so that material microstructure/properties are not altered by the joining process; (b) the heat-affected zone (HAZ) in which material microstructure/properties are effected only by the thermal effects associated with FSW. While this zone is normally found in the case of fusion welds, the nature of the microstructural changes may be different in the FSW case due to generally lower temperatures and a more diffuse heat source; (c) the thermo-mechanically affected zone (TMAZ) which is located closer than the HAZ zone to the butting surfaces. Consequently both the thermal and the mechanical aspects of the FSW affect the material microstructure/properties in this zone. Typically, the original grains are retained in this zone although they may have undergone severe plastic deformation; and (d) the weld *nugget* which is the innermost zone of an FSW joint. As a result of the way the material is transported from the regions ahead of the tool to the wake regions behind the tool, this zone typically contains the so-called "onion-ring" features. The material in this region has been subjected to most severe conditions of plastic deformation and high temperature exposure and consequently contains a very fine dynamically recrystallized (equiaxed-grain microstructure).

The FSW joint quality is typically affected by the following welding/process parameters: (a) rotational and transverse velocities of the tool; (b) tool-plunge depth; (c) tool tilt-angle; and (d) tool-design/material. Since, in general, higher temperatures are encountered in the case of higher rotational and lower transverse tool velocities, it is critical that a delicate balance between these two velocities is attained. Specifically, if the temperatures in the weld region are not high enough and the material has not been sufficiently softened, the weld zone may develop various flaws/defects arising from low ductility of the material. Conversely, when the temperatures are too high undesirable changes in the material microstructure/properties may take place and possibly incipient-melting flaws may be created during joining. To ensure that the necessary level of shoulder/work-piece contact pressure is attained and that the tool fully penetrates the weld, the tool-plunge depth (defined as the depth of the lowest point of the shoulder below the surface of the welded plate) has to be set correctly. Typically, insufficient tool-plunge depths result in low-quality welds (due to inadequate forging of the material at the rear of the tool), while excessive tool-plunge depths lead to under-matching of the weld thickness compared to the base material thickness. Tool rearward tilting by 2-4° has been often found to be beneficial since it enhances the effect of the forging process (Ref 18, 19).

FSW process has been investigated extensively using experimental means over the last two decades. The research carried out helped gain a better understanding of the FSW joining mechanisms and the accompanying evolution of the welded-material microstructure/properties (Ref 20-23), as well as it helped rationalize the effect of various FSW process parameters on the weld quality/integrity (Ref 13, 24-26). It should be recognized, however, that the aforementioned experimental efforts were able to only correlate the *post-mortem* welded-materials microstructure/properties with the FSW process parameters and provided relatively little real-time insight into the physics of heat/mass transfer and microstructure-evolution processes. As shown in our previous work (Ref 27-30), this insight can be gained by carrying out a detailed physically based computational investigation of the

FSW process. A detailed review of the prior research efforts dealing with numerical investigations of the FSW process reported in the public domain literature was conducted in our previous work (Ref 27-30). Hence, no overview of the prior computational FSW research efforts will be presented here.

The main objective of the present work is to combine the fully coupled thermo-mechanical finite-element analysis of the FSW process, developed in our previous work (Ref 27-30), with the basic physical metallurgy of two wrought aluminum alloys to predict/assess their FSW behaviors. The two alloys selected are AA5083-H131 (a solid-solution strengthened and strain-hardened/stabilized Al-Mg alloy) and AA2139 (a precipitation hardened quaternary Al-Cu-Mg-Ag alloy). Both of these alloys are currently being used in military-vehicle hull structural and armor systems. The operation and interaction of various microstructure-evolution processes taking place during FSW (e.g., extensive plastic deformation, dynamic re-crystallization, precipitates coarsening, over-aging, dissolution, and re-precipitation) will be considered to predict the material microstructure/properties in the various FSW zones of the two alloys.

The organization of the article is as follows: The key physical metallurgy aspects of the two alloys (AA5083 and AA2139) are reviewed in Section 2. The fully coupled thermo-mechanical analysis used in the computational investigation of the FSW process is presented in Section 3. Development and parameterization of two hardness models one for AA5083 and the other for AA2139 proposed within the present work and a comparison between the corresponding computed results and their experimental counterparts are discussed in Section 4. The main conclusions resulting from the present study are summarized in Section 5.

2. Physical Metallurgy of AA2139 and AA5083

2.1 AA5083-H131 Alloy: Microstructure and Properties

Wrought aluminum alloys (AA) are divided into seven major classes according to their principle alloying elements. The Al-Mg five-thousand series alloys possess high *rollability*, they are readily available as plates and, due to their high corrosion resistance and relatively high strength and good welding quality, they are often used in various structural and armor applications.

While often age-hardened Al-alloys (e.g., AA2139) are friction-stir welded, the microstructure evolution of these alloys during FSW is expected to be substantially more complex due to unstable nature of its precipitates (i.e., precipitates can coarsen, transform into more stable precipitates, or undergo partial or complete dissolution during alloy exposure to high temperature and can reappear on cooling in different morphologies and number densities, and even precipitates with different crystal structures may appear). The non-age-hardenable AA5083 (nominal chemical composition: 4.5 wt.% Mg, 0.25 wt.% Cr, and 0.75 wt.% Mn) is an Mg/Mn solid-solution hardened alloy and, in addition, in its H131 temper state is cold-work hardened and stabilized (to obtain a needed level of aging/over-aging resistance). While Al_6Mn precipitates are present in this alloy, due to aforementioned stabilizing heat treatment, they are relatively resistant to both dissolution and coarsening so that precipitate portion of the material microstructure can be taken as mainly unchanged during FSW.

It should be also noted that AA5083 is often used in aerospace and automotive industries for production of structural components with highly complex shapes. In these cases, the alloy is processed using super-plastic forming (a high temperature, low deformation rate, low forming pressure, open/close-die forming process). After relatively severe cold-working treatment, the alloy is recrystallized. The presence of very fine Al_6Mn precipitates promotes/stimulates grain nucleation during the recrystallization process resulting in an ultra-fine grain microstructure. Such microstructure enables plastic deformation by grain-boundary sliding and provides super-plastic behavior to the material when deformed under low deformation rate/high temperature conditions. Since, the material residing in the nugget FSW region is normally subjected to very high levels of plastid deformation and tends to recrystallize dynamically, one would expect formation of a very fine-grain microstructure in this region.

2.2 AA2139 Alloy: Age Hardening Behavior

AA2139 is an age-hardenable quaternary Al-Cu-Mg-Ag alloy characterized by a high (4-10) Cu/Mg ratio whose chemical composition places it into the α (an Al-based solid solution), $+S$ (an Al-Cu-Mg-based precipitate) and $+\theta$ (a Cu_2Al-based precipitate) equilibrium phase region. Ag additions are found to promote formation of metastable Ω precipitates during artificial aging over other competing precipitates such as S' and θ' (Ref 31). Since Ω precipitates tend to form on $\{111\}_\alpha$ planes (the slip planes in the Al-based alloys) they tent to impart the highest levels of strength to these alloys (Ref 32-36).

It is well established that during aging of Al-Cu-Mg-Ag alloys the following sequence of formation of metastable and stable precipitates is followed (Ref 31, 37):

$$\text{GP-zones} \rightarrow \theta'' \rightarrow \theta' + \Omega \rightarrow \theta' + S' \rightarrow S + \theta$$

where GP-zones stands for the Guinier-Preston zones, i.e., the clusters of Cu atoms on $\{100\}_\alpha$ planes which form in the earliest stages of aging of the supersaturated α-solid solution. It is also well established that high Cu/Mg ratios in these alloys tend to enhance relative stability of the Ω-phase with respect to that of the competing S' phase (Ref 31, 37). This finding is highly critical since, the best overall combination of mechanical properties in AA2139 is associated with the presence of Ω-phase precipitates.

Detailed microstructural investigations of the Ω-phase precipitates in AA2139 and related alloys over the last 10 years have established the following defining features of this microstructural constituent:

(a) Ω-phase precipitates form coherently within the α-solid solution with $(111)_\alpha$ planes acting as the habit planes;
(b) The crystal structure of this phase has been determined as being an Al_2Cu-base orthorhombic structure (Ref 33, 35, 38);
(c) The Ω phase tends to precipitate mainly in a homogeneous manner throughout the grain interior and predominantly in dislocation-free regions;
(d) Maximum temperature at which Ω phase can still exist is about 250 °C (Ref 39); and
(e) Ω-phase precipitates are most often present in hexagonal plate-like form with a typical thickness and in-plane dimensions of 2-3 nm and 100-200 nm, respectively (Ref 31-35, 38-40).

In addition to Ω-phase precipitates, the AA2139 alloy, in the peak age-hardened temper condition, also contains θ′-phase precipitates. Detailed examination of this type of precipitates over the last 10 years established the following (Ref 41, 42):

(a) These precipitates mainly form on $(100)_\alpha$ habit planes (Ref 34, 43);
(b) The θ′-phase precipitates are most often of octagonal-platelet or ellipsoidal shapes and their size is comparable to that of the Ω-phase precipitates (Ref 43, 44);
(c) The θ′ phase possesses a body-centered tetragonal crystal structure; and
(d) Since S' precipitates are semi-coherent with the α-matrix, they tend to preferentially form on dislocations and low-angle grain boundaries (Ref 33, 45).

While Ω-phase and θ′-phase precipitates can normally co-exist in the AA2139-type of alloys, replacement of the Ω-phase precipitates with S'-phase precipitates (after prolonged aging) is of major concern. That is, as S'-phase precipitates form and gradually evolve into S-phase precipitates, they tend to take away Mg-Ag co-clustering surrounding Ω-phase precipitates leading to gradual dissolution of the Ω-phase precipitates (Ref 37). Numerous investigations of the S'-phase precipitates in AA2139 and related alloys revealed the following defining features of this microstructural constituent:

(a) The S'-phase precipitates tend to form both heterogeneously on dislocations and homogeneously throughout the grain interior (Ref 35);
(b) They generally appear as laths and are sometimes associated with $(120)_\alpha$ habit planes (Ref 33); and
(c) The average S'-phase precipitate size is generally comparable to that of the Ω-phase and θ′-phase precipitates (Ref 35).

In addition to the metastable and stable precipitates mentioned above whose formation is driven by the thermodynamic driving forces to reduce the extent of super saturation from the as-quenched α-phase solid solution, fine-scale Mn- or Zr-rich dispersoids are also present in AA2139 type alloys. These dispersoids are result of relatively low solubility of Mn and Zr in Al and tend to form (and, hence, to survive) at substantially higher temperatures than the aforementioned precipitates. Typically the so-called T-phase dispersoids are found in AA2139. The main defining features of this phase are:

(a) Its stoichiometric formula is $Al_{20}Mg_2Mn_3$ (Ref 33);
(b) The T phase possesses an orthorhombic crystal structure (Ref 35);
(c) It is mainly present in a rod form with the rod length between 50 and 500 nm (Ref 31);
(d) While finer T-phase dispersoids generally lead to higher static strength levels in the AA2139-type alloys, coarser T-phase dispersoids tend to improve strain-localization resistance and, thus, improve dynamic strength of the material (Ref 31); and
(e) While both Zr and Mn tend to promote formation of the T-phase dispersoids, Mn generally yields coarser dispersoids and is, hence, a preferred alloying element from the standpoint of achieving improved dynamic strength in AA2139.

3. Computational Analysis of the FSW Process

As mentioned earlier, modeling of the FSW process carried out in the present work employed the fully coupled thermo-mechanical finite-element procedure developed in our prior work (Ref 27-30). Since a detailed account of the procedure was provided in Ref 27-30, only a brief overview of it will be presented in the remainder of this section.

3.1 Computational Domain

The computational domain used consists of a (40.0-mm radius, 3.0-mm thickness) circular plate (with a concentric through-the-thickness 3.0-mm radius circular hole) and a two-part tool (consisting of a 3.0-mm radius, 3.0-mm length solid right circular cylinder, at the bottom, and a 9.0-mm radius, 3.0-mm thickness circular-plate section, on the top), Fig. 2(a, b). The computational domain is meshed using ~20,000 first-order eight-node reduced-integration hexahedral thermo-mechanically coupled solid elements (the meshed model is not shown for brevity).

3.2 Computational Algorithm

The FSW process is analyzed computationally using a fully coupled thermo-mechanical finite-element algorithm within which heat dissipation associated with plastic deformation and tool/work-piece interfacial friction-sliding is treated as a source in the governing thermal equation while the effect of temperature on the mechanical response of the work-piece material is taken into account through the use of a temperature-dependent work-piece material model.

The analysis is carried out by prescribing from the onset a constant rotational velocity and a constant downward pressure to the tool. Instead of assigning a travel velocity to the tool along the (postulated) butting surfaces of the work-piece, the work-piece material is forced to move through the work-piece computational domain at the same velocity but in the opposite

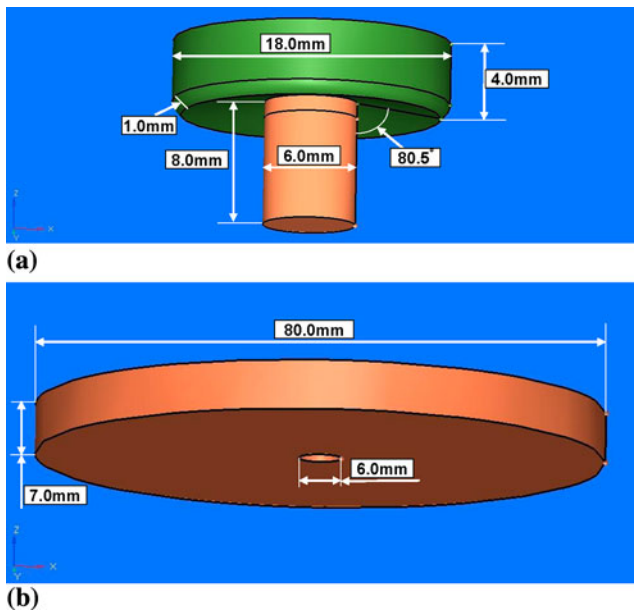

Fig. 2 Geometrical models with dimensions for the (a) FSW tool and (b) FSW work-piece

direction. Thus, Fig. 2(b) represents not the entire work-piece but rather a circular region around the tool in the otherwise infinitely long/wide work-piece. During the FSW process simulation, the material is prevented from flowing through the bottom face of the work-piece computational domain (to mimic the effect of rigid work-piece backing plate), standard convective boundary conditions are applied over free surfaces of the work-piece and the tool while enhanced convection boundary conditions are applied over the bottom face of the work-piece (to mimic the effect of enhanced heat extraction through the work-piece backing plate).

Work-piece/tool interactions are accounted for through the use of a penalty algorithm within which the extent of contact pressure is governed by the local surface penetrations while shear stresses are transferred via a "slip/stick" algorithm, that is shear stresses lower than the frictional shear stress are transferred without interface sliding (otherwise interface sliding takes place). The frictional shear stress is defined by a modified Coulomb law within which there is an upper limit to this quantity (set equal to the shear strength of the work-piece material). The frictional shear stress is then defined as a smaller of the product between the static/kinetic friction coefficient and the contact pressure, on one hand, and the work-piece material shear strength, on the other.

As mentioned earlier, both plastic deformation and frictional sliding are treated as heat sources. To account for the fact that a small fraction of the plastic-deformation work is stored in the form of crystal defects, 95% of this work was assumed to be dissipated in the form of heat. As far as heat generation due to frictional sliding is concerned, it is assumed that its rate scale with the product of local interfacial shear stress and the sliding rate, and that 100% of this energy is dissipated in the form of heat. Partitioning of this heat between the tool and the work-piece is then computed using the appropriate thermal properties of the two materials.

As established earlier, work-piece material in the nugget and TMAZ regions experience large plastic deformations during FSW under these circumstances, the use of a Lagrangian approach in which the finite-element mesh is attached to and moves with the material may display serious numerical problems (due to excessive mesh distortion). To overcome this approach, an Arbitrary Lagrangian-Eulerian (ALE) formulation is used within which adaptive re-meshing is carried out to maintain good quality mesh.

The fully coupled thermo-mechanical problem dealing with FSW is solved using an explicit solution algorithm implemented in ABAQUS/Explicit (Ref 46), a general purpose finite element solver. To keep the computational cost reasonable while ensuring stability and robustness of the computational procedure, a mass scaling algorithm is used. This algorithm adaptively adjusts material density in the critical finite elements without significantly affecting accuracy of the computational results.

3.3 Material Models

Since the tool normally experiences relatively lower deformation during FSW, it is modeled using a rigid material. Its density and thermal properties are next set to that of AISI-H13, a hot-worked tool steel, frequently used as the FSW-tool material.

The work-piece material is assumed to be isotropic, linear-elastic and strain-hardenable, strain-rate sensitive, thermally softenable plastic material and is modeled using Johnson-Cook material model (Ref 47). Standard density and thermal properties for AA5083 and AA2139 alloys are used to define the thermal-portion of the material model.

While in the original Johnson-Cook material model temperature is assumed to affect the material strength through its effect on thermal activation of dislocation motion, nugget zone material exposure to high temperature during FSW is found to result in dynamic recrystallization since this phenomenon is not accounted for the original Johnson-Cook model, a modified version of this model was proposed in our prior work (Ref 27-30). Essentially, strain hardening is still assumed to be related to the effective plastic strain, $\bar{\varepsilon}_{pl}$, via a parabolic relation, $B\bar{\varepsilon}_{pl}^{n}$, where B and n are material parameters. However, $\bar{\varepsilon}_{pl}$ is taken to be composed of two terms: one (positive) associated with the operation of plastic deformation and the other (negative) resulting from the operation of dynamic recrystallization.

3.4 Typical Results

In this section, a few typical FSW process simulation results are presented and briefly discussed.

3.4.1 Equivalent Plastic Strain Field. An example of the typical results pertaining to spatial distribution and temporal evolution of the equivalent plastic strain in the work-piece during FSW is displayed in Fig. 3(a, b). Simple examination of the results displayed in these figures and of the results obtained in the present work (but not shown for brevity) reveals that:

(a) Typically, plastic strains in a 20 and 50% range are observed with the strain magnitude being controlled by FSW process conditions such as tool contact pressure, tool rotational, and translational speeds;
(b) The highest equivalent plastic strains are always found in the work-piece material right below the tool shoulder and equivalent plastic strains progressively decreased from this region as a function of the distance in the radial and through-the-thickness directions;
(c) Distribution of the equivalent plastic strains is highly asymmetric. This asymmetry is related to the differences in the material transport (at the advancing and the retreating sides of the weld) from the region ahead of the tool to the region behind the tool; and
(d) Typically, equivalent plastic strain differences between the top and bottom surfaces of the work-piece are reduced while equivalent plastic strain magnitudes are increased as the tool translational speed is decreased and the tool/work-piece contact pressure is increased. This finding suggests that under these FSW process conditions the extent of material stirring/mixing (which plays a critical role in weld quality/joint strength) is increased.

3.4.2 Nodal Velocity Field. The distribution of nodal velocities at the outer surfaces of the work-piece at two different times (0.0 and 0.5 s) is displayed in Fig. 3(c, d). For clarity, the tool is not shown. These figures clearly show that the initially assigned unidirectional velocity field in the direction of welding, quickly transforms into the velocity field in which there is a well-defined stir region right below the shoulder (within which the material circles around the pin) and the remainder of the field (within which the material tends to flow around the stir region). A comparison of the results

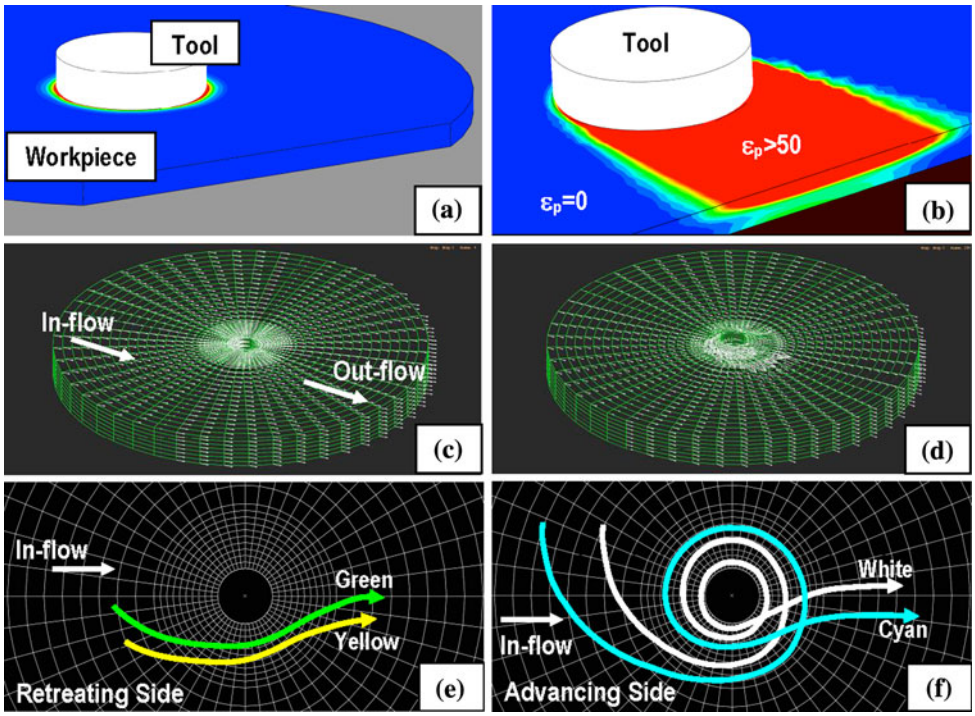

Fig. 3 Typical FSW computational-analysis results pertaining to the steady-state distribution of (a, b) equivalent plastic strain, (c, d) nodal velocities, and (e, f) retreating-side and advancing-side tracer-particle trajectories

displayed in Fig. 3(c, d) clearly shows how the region underneath the tool shoulder which is initially unfilled becomes filled as FSW proceeds. Once the space under the shoulder is fully filled it remains filled as the FSW process continues. The material in this region is constantly being refreshed as the tool advances in the welding direction.

3.4.3 Material/Tracer-Particle Trajectories. It should be noted that the results displayed in Fig. 3(c, d) shows the spatial distribution and temporal evolution of the nodal velocities. Due to the ALE character of the finite-element analysis used in the present work, the motion of the finite-element mesh is not completely tied to the motion of the material. Consequently, the results displayed in Fig. 3(c, d) shows the velocities of the material particles which at that moment pass through the nodal points in question. However, one must recognize that at different times different material particles are associated with the same nodes. In order to observe stirring of the material under the tool shoulder, one should monitor particle trajectories rather than nodal velocities. This is possible within ABAQUS/Explicit through the use of so-called "tracer particles" which are attached to the material points (and not to the mesh nodal points).

Figure 3(e, f) shows typical results pertaining to the trajectory of retreating-side and advancing-side tracer particles, respectively. The tracer particles displayed in these figures are initially located in a plane, which is halfway between the top and bottom surfaces of the work-piece. For improved clarity, tracer-particle trajectories are color coded. The results displayed in Fig. 3(e, f) clearly revealed the following basic aspects of the FSW process:

(a) At the retreating side, work-piece material particles (as represented by the yellow and green tracer-particle trajectories, Fig. 3e), typically do not enter the stir zone under the tool shoulder and usually only flow around it;
(b) At the advancing side, work-piece material particles which are initially closer to the butting surfaces (as represented by the white and cyan tracer-particle trajectories, Fig. 3f), tend to passes over to the retreating side and get co-stirred with some of the retreating-side material particles to form the welded joint; and
(c) At the advancing side, work-piece material particles further away from the initial butting surfaces remain on the advancing side and either enter the stir region on the advancing side or flow around it.

4. Material Microstructure/Hardness Evolution

4.1 Qualitative Analysis of Hardening Mechanisms Within the FSW Joint

4.1.1 AA5083. Based on the discussion regarding the microstructure/property relations in AA5083 presented earlier in Section 2.1, the following strengthening mechanisms are expected to be present in this alloy: (a) solid-solution strengthening; (b) strain hardening; and (c) grain-size refinement. Relative importance of these mechanisms within the four weld-zones (e.g., the weld nugget, the TMAZ, the HAZ, and the base material) is discussed in the remainder of this section.

Solid-Solution Strengthening. This hardening mechanism is present in all four weld-zones and its contribution to the material hardness is expected to be fairly uniform across the entire weld region.

Strain Hardening. When AA5083 is in a H131 temper condition, strain-hardening mechanism provides a contribution to the material hardness in the base-metal zone which is larger than the contributions of the other two mechanisms. In the HAZ, some annealing will take place. However, since this annealing is primarily due to recovery or polygonization, the contribution of strain hardening to the material hardness in this region will remain quite comparable to that in the base-metal region. The contribution of strain hardening to the overall material hardness in the TMAZ is expected to increase since the material in this region typically experiences significant levels of plastic deformation. In the weld nugget region, material microstructure and properties are dominated by dynamic recrystallization and, hence, the contribution of strain hardening to the overall material hardness in this region is minimal.

Grain-Size Refinement. Since, to a first-order approximation, the average grain size does not change between the base-metal zone, the HAZ, and the TMAZ, the contribution of this strengthening mechanism to the overall material strength is expected to be comparable in these three weld-zones. On the other hand, dynamic recrystallization yields a very fine-grain structure within the nugget zone so that the overall contribution of the grain-refinement mechanism to the material hardness is expected to be largest in this weld zone.

4.1.2 AA2139. Based on the discussion regarding the microstructure/property relations in AA2139 presented earlier in Section 2.2, the following strengthening mechanisms are expected to be present in this alloy: (a) precipitation hardening; (b) strain hardening; and (c) grain-size refinement. Relative importance of the strain hardening and the grain-size refinement mechanisms within the four weld-zones was discussed earlier in the context of AA5083. The main points made at that time are equally valid in the case of AA2139. As far as the role of the precipitation hardening mechanism in AA2139 is concerned, the following main observations can be made. When AA2139 T8 (quenched + cold worked + artificially aged) temper condition, precipitation hardening provides a contribution to the material hardness in the base-metal zone which is larger than the contributions of the other two mechanisms. In general, material exposure to high temperatures within the remaining three main weld-zones causes over-aging and the associated loss in material strength. This loss increases in its extent as one approaches the original weld line, i.e., as one moves through the HAZ, then through the TMAZ and ultimately through the weld nugget.

4.2 Simple Models and Parameterization for Hardening Mechanisms Within the FSW Joint

4.2.1 AA5083. The following simple model for the hardness of AA5083, H, is proposed in the present work:

$$H = H_C(C) + \frac{H_d}{d^{1/2}} + H_\varepsilon \bar{\varepsilon}^n, \qquad \text{(Eq 1)}$$

where the three terms on the right-hand side of Eq (1) represents, respectively, the contributions of solid-solution strengthening, grain-size refinement, and strain hardening to material hardness, C is the alloying elements content, d is the average grain size, and $\bar{\varepsilon}$ is the equivalent plastic strain while H_C, H_d, H_ε, and n are the hardness-model parameters.

In accordance with the previous discussion, solid-solution hardness parameter H_C is considered as constant throughout all four zones of the weld. Using the hardness data for fully annealed coarse grained AA5083 (Ref 48) (in which the contributions of grain-size refinement and strain hardening are minimal) H_C is assessed as 410 MPa.

The grain-refinement hardening term in Eq (1) is written in accordance with the Hall-Petch relation (Ref 49). Using the results regarding grain-size dependence of hardness in fully annealed AA5083 (Ref 50), H_d is evaluated as 340 MPa.

The last term on the right-hand side of Eq (1) is modeled as a parabolic strain-hardening law (Ref 47). A linear regression analysis of the strain-hardening data reported in Ref 51, yielded H_d = 620 MPa and n = 0.23.

4.2.2 AA2139. To account for the precipitation-hardening effects in AA2139, hardness in this alloy is modeled as:

$$H = [H_O + \Delta H_{PA}(1 - \eta)] + \frac{H_d}{d^{1/2}} + H_\varepsilon \bar{\varepsilon}^n, \qquad \text{(Eq 2)}$$

where the first term on the right-hand side of Eq (2) represents the contribution of precipitation hardening, H_O and ΔH_{PA} are hardness levels in the over-aged condition and hardness increment at the peak-aged condition, respectively, and η is the extent of over-aging. Using the available data for hardness variation during aging heat treatments (Ref 52), H_O and ΔH_{PA} are assessed as 420 and 790 MPa, respectively.

Due to a lack of available data in the open literature pertaining to the effect of grain-size refinement and strain hardening on the hardness in AA2139, the hardness-model parameters for these two strengthening mechanisms are set equal to their AA5083 counterparts reported above. Furthermore, the contribution of solid-solution strengthening to the hardness of AA2139 is neglected since it is expected to be small in comparison to the contributions associated with the other three strengthening mechanisms.

4.3 Material State-Variable Evolution Equations

In the previous section, the two hardness models (one for AA5083 and the other AA2139) were parameterized. Within these models, the state of the material microstructure was represented by three state variables: (a) the degree of over-aging, η (applicable only in case of AA2139); (b) the average grain size, d; and (c) the equivalent plastic strain, $\bar{\varepsilon}$. To apply Eq (1), (2), i.e., to compute material hardness at different locations within the weld, one must compute the final values of these three state variables. This is done for each material point by integrating, over the entire thermo-mechanical history, the appropriate evolution equations (provided below) for the three state variables starting from their initial values (in the base metal before welding).

4.3.1 Degree of Over-Aging. Starting with a simple inverse exponential law for the temporal evolution of the extent of over-aging under isothermal conditions, $\eta = e^{-t/\tau_0}$, where t is time and τ_0 is a temperature-dependent relaxation time. Carrying out the appropriate chain-rule differentiation and simplification, the following evolution equation for the degree of over-aging is proposed:

$$\frac{d\eta}{dt} = e^{\frac{-C_1\eta}{1-\eta}} \frac{C_2}{1 - T_H^m} \quad 0 \le \eta \le 1.0, \qquad \text{(Eq 3)}$$

where $0 \le T_H \le 1.0$ is a room/melting temperature-based homologous temperature, $T_H = (T - T_{Room})/(T_{Melt} - T_{Room})$ and C_1, C_2, and m are material parameters. Using available aging kinetics data at different temperatures (Ref 2) C_1, C_2, and m are assessed as 0.8, 0.00035, and 9.6, respectively.

It should be noted that within the present model for material over-aging, this phenomenon is assumed to be solely controlled by material exposure to high temperatures while the potential effect of plastic deformation on the over-aging kinetics is treated as a second-order effect and, hence, ignored.

4.3.2 Grain-Size Evolution Function. Grain-size evolution is assumed to be controlled by collective contributions of plastic-deformation and dynamic-recrystallization processes. Plastic deformation does not per se alter the grain size but creates dislocations which rearrange themselves into low-angle grain boundaries to form sub-grains. As new dislocations are generated and incorporated into the sub-grain boundaries, mis-orientation between the sub-grains increases. At some point, the degree of mis-orientation becomes large enough to convert a sub-grain into a grain (with large-angle grain boundaries) which then begins to consume the surrounding sub-grains until it encounters another "recrystallized" grain. The rate of dislocation incorporation into the sub-grain boundaries and the rate of growth of "recrystallized" grains are thermally activated, i.e., they depend on temperature via an Arrhenius-type relation. Taking all this into account, and following a procedure similar to that employed in the case of over-aging, the following grain-size evolution law is proposed here:

$$\frac{dd}{dt} = (1 - e^{-C_3 d})\frac{C_4 \varepsilon^p}{1 - T_H^q}, \qquad \text{(Eq 4)}$$

where d is the average grain size and C_3, C_4, p, and q are material parameters. Using available recrystallization kinetics data at different temperatures (Ref 53) C_3, C_4, p, and q are assessed as 0.00051/μm, 0.24 μm/s, 0.71 and 0.97, respectively.

4.3.3 Equivalent Plastic Strain Evolution Function. The equivalent plastic strain used in the present work is identical to the one developed in our recent work (Ref 27-30). Since a detail account of the derivation procedure for this equation can be found in Ref 27-30, only a brief overview of this procedure will be provided in the remainder of this section.

In the absence of dynamic-recrystallization effects, evolution of the equivalent plastic strain is determined by simultaneously satisfying the Hooke's law, yield criterion and flow rule relations, at each material point during each time increment (Ref 27-30). In this way, only the effect of strain hardening due to an increase in the dislocation density and the resulting increase in the dislocation-motion resistance imposed by the surrounding dislocations on the material hardness/strength is taken into account. To include the effects of dynamic recrystallization when dynamic recrystallization accompanies plastic deformation, the equivalent plastic strain evolution equation has to be modified to include the associated annealing effects. In other words, an additional (negative) equivalent plastic strain-rate term has to be used to account for the dynamic-recrystallization effects. This additional term is based on the following physics-based arguments:

(a) Dynamic recrystallization is a thermally activated process and consequently the correction term in the equivalent plastic strain evolution equation must contain a Boltzmann probability term in the form $\exp(-Q/RT)$, where Q is an activation energy while R is the universal gas constant. In other words, the dynamic-recrystallization correction term in the equivalent plastic strain evolution equation should be an Arrhenius-type function;
(b) Since the rate of recrystallization across various alloy systems appear to scale with the previously defined homologous temperature, T_h, this term was replaced with Q/RT term in the Boltzmann probability relation with q/T_h, where q is a dimensionless activation energy; and
(c) Due to the fact that the rate at which material tends to recrystallize increases as the amount of cold work is increased, q was set to be a decreasing function of the equivalent plastic strain $\bar{\varepsilon}$.

Based on these arguments, the dynamic-recrystallization contribution to the evolution of the equivalent plastic strain was expressed as:

$$\dot{\bar{\varepsilon}}_{pl,dyn\_rec} = \dot{\bar{\varepsilon}}_{o,pl,dyn\_rec} e^{\left(-q(\bar{\varepsilon}_{pl})/T_h\right)}, \qquad \text{(Eq 5)}$$

where $\dot{\bar{\varepsilon}}_{o,pl,dyn\_rec}$ is a dynamic-recrystallization frequency/pre-exponential term. An analysis of the available experimental data pertaining to the kinetics of recrystallization of AA5083 (Ref 27-30) showed that q scales inversely with $\bar{\varepsilon}_{pl}$ raised to a power of 2.9. Based on this finding and using the curve-fitting results for the experimental recrystallization kinetics data reported in Ref 53, it is found that Eq (5) can be rewritten as:

$$\dot{\bar{\varepsilon}}_{pl,dyn\_rec} = 21.5 e^{-1/(\bar{\varepsilon}_{pl}^{2.9} T_h)} \qquad \text{(Eq 6)}$$

4.4 Computational Results and Comparison with the Experimental Counterparts

The models for the evolution of material hardness (as well as that for the evolution of the material average grain size) are used in conjunction with the FSW process analysis results (provides the required thermo-mechanical history input, i.e., the temporal variation of temperature and equivalent plastic strain of the material points within the weld) to compute variations in the material hardness and grain size across the four weld-zones. These results are next compared with their experimental counterparts in order to help validate the models developed in the present work.

4.4.1 AA5083. Variation of the material hardness measured transversely across the friction-stir weld over the top surface of the work-piece consisting of AA5083-H131 plates on both sides of the joint is displayed in Fig. 4(a, b). The results displayed in these two figures correspond to two different welding tool traverse speeds: (a) Fig. 4(a) 100 mm/min and (b) Fig. 4(b), 150 mm/min, while the tool rotation speed, shoulder diameter, and threaded pin diameter are kept constant at 350 rpm, 18 mm, and 5 mm, respectively.

For comparison, the corresponding experimental results obtained in Ref 54 are also displayed in Fig. 4(a, b). Since the original hardness results reported in Ref 54 were given using Vicker's hardness units, they were converted using the known indentation loads and indentor geometry data to the SI stress units before including in these figures.

Simple examination of the results displayed in Fig. 4(a, b) shows that:

(a) The present hardness model yields a physically realistic variation in material hardness across the FSW joints, i.e., the computed hardness profiles clearly delineate the four different weld-zones.
(b) As far as the quantitative agreement between the present computed results and their counterparts from Ref 54

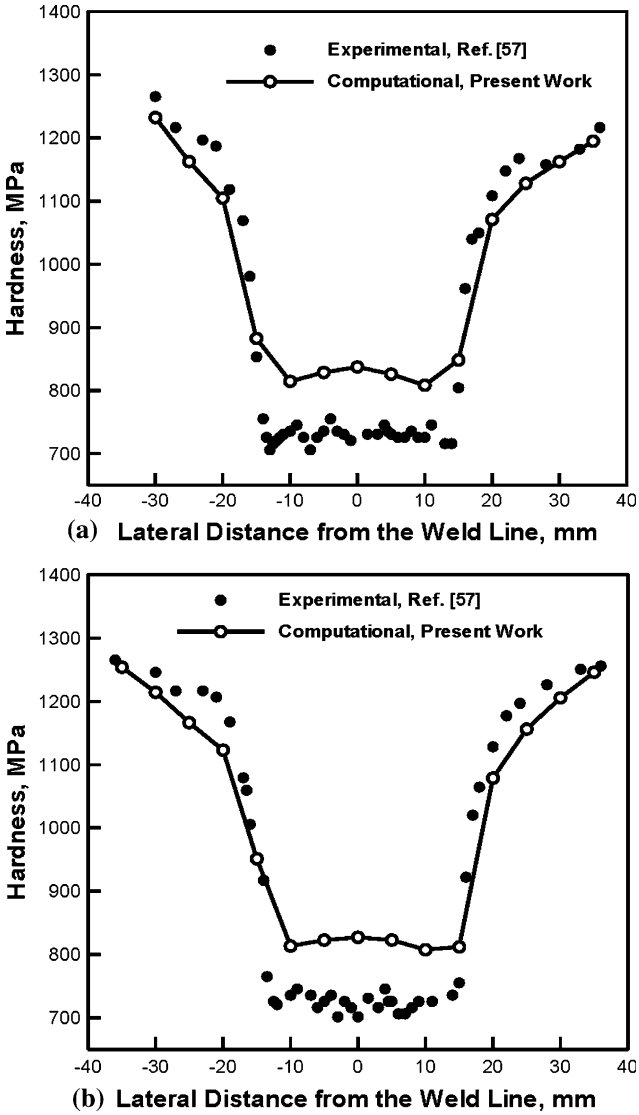

Fig. 4 A comparison between the computed and the experimental hardness (transverse) profiles over the top surface of the 5083 work-piece. Please see the text for details regarding the friction stir weld parameters associated with the results displayed in (a) and (b). Data pertaining to the advancing side of the weld joint are on the right-hand side of the plot

is concerned, it can be characterized as being good to fair. There may be many reasons for the observed discrepancy: (i) the functional relations used to describe the contribution of various mechanisms to material hardness can be further improved; (ii) available experimental data used for model parameterization were relatively scarce and came from different sources; and (iii) potential inaccuracies associated with hardness measurements in Ref 54.

In Fig. 5, a comparison is made between the grain size results obtained in the present computational analysis and their experimental counterparts obtained in Ref 55. Considering the fact that not all the FSW process parameters were specified in Ref 55, one should be encouraged by the level of agreement observed in Fig. 5 between the computed and the experimentally measured results.

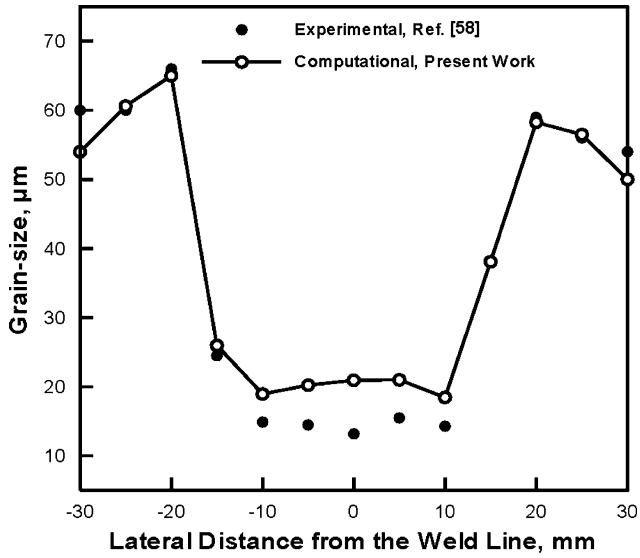

Fig. 5 A comparison between the computed and the experimental grain-size profiles over the top surface of the 5083 work-piece. Data pertaining to the advancing side of the weld joint are on the right-hand side of the plot

4.4.2 AA2139. A comparison of the computed results (pertaining to the hardness variation in a direction transverse to the original weld line) and their experimental counterparts obtained in Ref 56 in the case of two friction-stir-welded AA2139 plates is displayed in Fig. 6(a, c). The results displayed in Fig. 6(a, c) correspond, respectively, to the hardness measurements over the top surface of the work-piece, intermediate surface of the work-piece and over the bottom surface. In all three cases the same FSW process parameters (welding speed: 100 mm/min; tool rotational speed: 350 rpm; shoulder diameter: 18 mm; pin diameter: 5 mm) were used.

Simple examination of the results displayed in Fig. 6(a-c) shows that as in the case of AA5083, the present hardness model provides physically realistic hardness profiles in a direction transversely oriented with respect to the weld (at different locations through the thickness of the work-piece) and that the computational/experimental agreement is good to fair.

A comparison of the computed variation in the average grain size across the FSW joint and its experimental counterpart obtained in Ref 57 is displayed in Fig. 7. These results pertain to the top surface of the work-piece. Simple examination of the results displayed in Fig. 7 shows that the computation/experiment agreement is comparable to that obtained in the case of AA5083 (i.e., the agreement is acceptable).

5. Summary and Conclusions

Based on the work presented and discussed in the present work, the following main summary remarks and conclusions can be made:

1. A brief overview is provided of the key physical metallurgy aspects of AA5083 (a solid-solution strengthened and strain-hardened/stabilized Al-Mg-Mn alloy) and AA2139 (a precipitation hardened quaternary Al-Cu-Mg-Ag alloy).

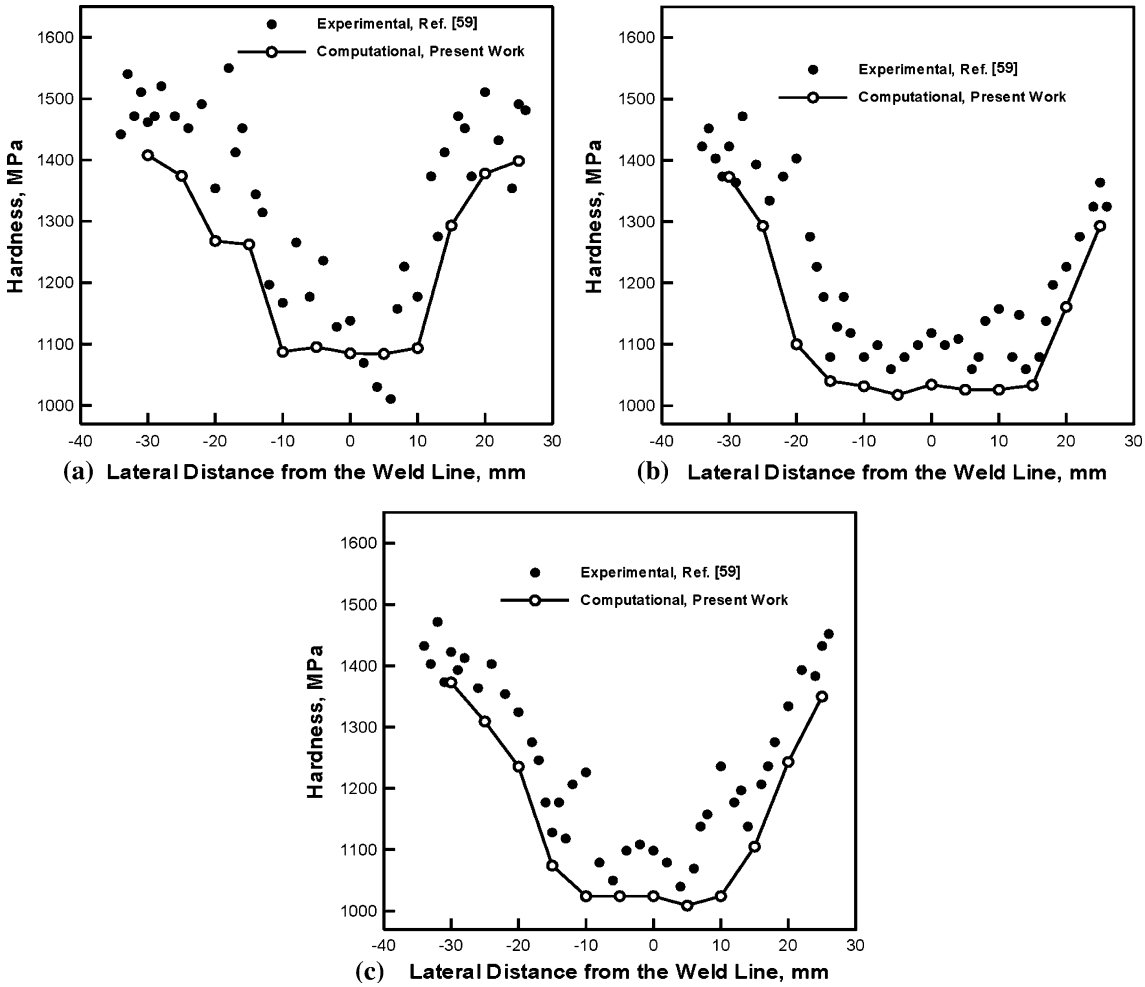

Fig. 6 A comparison between the computed and the experimental hardness profiles over a transverse cut through the 2139 work-piece weld: (a) top surface of the work-piece, (b) a half-way through the thickness section, and (c) the bottom surface of the work-piece. Please see the text for details regarding the friction stir welding parameters. Data pertaining to the advancing side of the weld joint are on the right-hand side of the plot

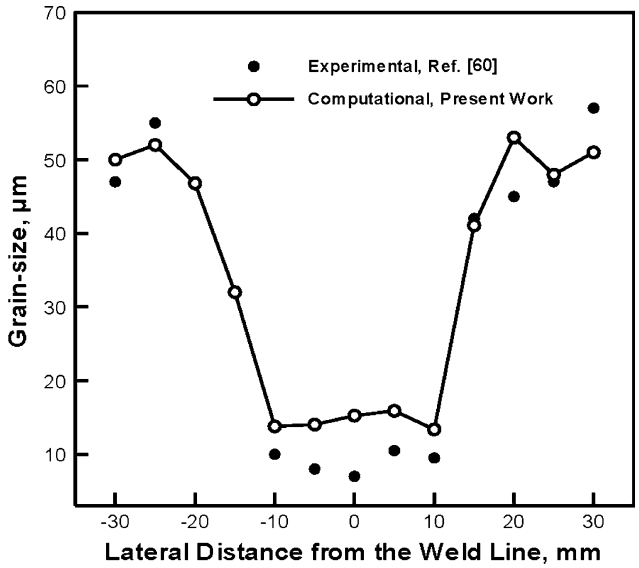

Fig. 7 A comparison between the computed and the experimental grain-size profiles over the top surface of the 2139 work-piece. Data pertaining to the advancing side of the weld joint are on the right-hand side of the plot

2. Simple mathematical models are developed and parameterized for the hardness evolution within various friction-stir-welded zones (e.g., the weld nugget, the TMAZ, and the HAZ) for the two alloys in question.
3. Integration of the hardness and grain-size evolution equations over the thermo-mechanical history of various material points within the weld yielded a hardness/grain-size profile (one for each alloy) in a direction transverse to the weld line. The thermo-mechanical history information was obtained by carrying out a fully coupled thermo-mechanical finite-element analysis of the FSW process.
4. A comparison of the computed hardness and grain-size profiles with their experimental counterparts showed that the proposed approach can account qualitatively quite well for the measured behavior while quantitative agreement between the computed and experimental results is only fair.

Acknowledgment

The material presented in this article is based on work supported by the U.S. Army/Clemson University Cooperative Agreements W911NF-04-2-0024 and W911NF-06-2-0042.

References

1. "Armor Plate, Aluminum Alloy, Weldable 5083 and 5456," MIL-DTL-46027J, U.S. Department of Defense, Washington DC, August 1992
2. A. Cho, Alcan Rolled Products, Ravenswood, WV, Private Communication, June 2009
3. "Armor Plate, Aluminum Alloy, 7039," MIL-DTL-46063H, U.S. Department of Defense, Washington DC, December 1992
4. "Aluminum Alloy Armor, 2219, Rolled Plate and Die Forged Shapes," MIL-DTL-46118E, U.S. Department of Defense, Washington DC, August 1998
5. "Aluminum Alloy Armor Rolled Plate (1/2 to 4 Inches Thick), Weldable (Alloy 2519)," MIL-DTL-46118E, U.S. Department of Defense, Washington DC, February 2000
6. W.M. Thomas, E.D. Nicholas, J.C. Needham, M.G. Murch, P. Temple-Smith, and C.J. Dawes, Friction Stir Butt Welding, International Patent Application No. PCT/GB92/02203, 1991
7. C.J. Dawes and W.M. Thomas, Friction Stir Process Welds Aluminum Alloys, *Weld. J.*, 1996, **75**, p 41–52
8. W.M. Thomas and R.E. Dolby, Friction Stir Welding Developments, *Proceedings of the Sixth International Trends in Welding Research*, S.A. David, T. DebRoy, J.C. Lippold, H.B. Smartt, and J.M. Vitek, Ed., ASM International, Materials Park, OH, 2003, p 203–211
9. J.H. Cho, D.E. Boyce, and P.R. Dawson, Modeling Strain Hardening and Texture Evolution in Friction Stir Welding of Stainless Steel, *Mater. Sci. Eng. A*, 2005, **398**, p 146–163
10. H. Liu, H. Fulii, M. Maeda, and K. Nogi, Tensile Properties and Fracture Locations of Friction-Stir Welded Joints of 6061-T6 Aluminium Alloy, *J. Mater. Sci. Lett.*, 2003, **22**, p 1061–1063
11. W.B. Lee, C.Y. Lee, W.S. Chang, Y.M. Yeon, and S.B. Jung, Microstructural Investigation of Friction Stir Welded Pure Titanium, *Mater. Lett.*, 2005, **59**, p 3315–3318
12. W.M. Thomas and E.D. Nicholas, Friction Stir Welding for the Transportation Industries, *Mater. Des.*, 1997, **18**, p 269–273
13. J.Q. Su, T.W. Nelson, R. Mishra, and M. Mahoney, Microstructural Investigation of Friction Stir Welded 7050-T651 Aluminum, *Acta Mater.*, 2003, **51**, p 713–729
14. O. Frigaard, Ø. Grong, and O.T. Midling, A Process Model for Friction Stir Welding of Age Hardening Aluminum Alloys, *Metall. Mater. Trans. A*, 2001, **32**, p 1189–1200
15. M.W. Mahoney, C.G. Rhodes, J.G. Flintoff, R.A. Spurling, and W.H. Bingel, Properties of Friction-Stir-Welded 7075 T651 Aluminum, *Metall. Mater. Trans. A*, 1998, **29**, p 1955–1964
16. C.G. Rhodes, M.W. Mahoney, W.H. Bingel, R.A. Spurling, and C.C. Bampton, Effect of Friction Stir Welding on Microstructure of 7075 Aluminum, *Scr. Mater.*, 1997, **36**, p 69–75
17. G. Liu, L.E. Murr, C.S. Niou, J.C. McClure, and F.R. Vega, Microstructural Aspects of the Friction-Stir-Welding of 6061-T6 Aluminum, *Scr. Mater.*, 1997, **37**, p 355–361
18. K.V. Jata and S.L. Semiatin, Continuous Dynamic Recrystallization During Friction Stir Welding, *Scr. Mater.*, 2000, **43**, p 743–748
19. K. Masaki, Y.S. Sato, M. Maeda, and H. Kokawa, Experimental Simulation of Recrystallized Microstructure in Friction Stir Welded Al Alloy Using a Plane-Strain Compression Test, *Scr. Mater.*, 2008, **58**, p 355–360
20. W.M. Thomas, E.D. Nicholas, J.C. NeedHam, M.G. Murch, P. Templesmith, and C. J. Dawes, Friction Stir Welding, International Patent Application No. PCT/GB92102203 and Great Britain Patent Application No. 9125978.8, 1991
21. R.S. Mishra and Z.Y. Ma, Friction Stir Welding and Processing, *Mater. Sci. Eng. R. Rep.*, 2005, **50**, p 1–78
22. H.W. Zhang, Z. Zhang, and J.T. Chen, The Finite Element Simulation of the Friction Stir Welding Process, *Mater. Sci. Eng. A*, 2005, **403**, p 340–348
23. A.J. Ramirez and M.C. Juhas, Microstructural Evolution in Ti-6Al-4V Friction Stir Welds, *Mater. Sci. Forum*, 2003, **426–432**, p 2999–3004
24. H.G. Salem, A.P. Reynolds, and J.S. Lyons, Microstructure and Retention of Superplasticity of Friction Stir Welded Superplastic 2095 Sheet, *Scr. Mater.*, 2002, **46**, p 337–342
25. H.J. Liu, Y.C. Chen, and J.C. Feng, Effect of Zigzag Line on the Mechanical Properties of Friction Stir Welded Joints of an Al-Cu Alloy, *Scr. Mater.*, 2006, **55**, p 231–234
26. Z.Y. Ma, S.R. Sharma, and R.S. Mishra, Effect of Friction Stir Processing on the Microstructure of Cast A356 Aluminum, *Mater. Sci. Eng. A*, 2006, **433**, p 269–278
27. M. Grujicic, T. He, G. Arakere, H.V. Yalavarthy, C.-F. Yen, and B.A. Cheeseman, Fully-Coupled Thermo-Mechanical Finite-Element Investigation of Material Evolution During Friction-Stir Welding of AA5083, *J. Eng. Manuf.*, 2009, **224**(4), p 609–622
28. M. Grujicic, G. Arakere, H.V. Yalavarthy, T. He, C.-F. Yen, and B.A. Cheeseman, Modeling of AA5083 Material-Microstructure Evolution During Butt Friction-Stir Welding, *J. Mater. Eng. Perform.*, 2010, **14**(5), p 672–684
29. M. Grujicic, G. Arakere, B. Pandurangan, A. Hariharan, C.-F. Yen, and B. A. Cheeseman, Development of a Robust and Cost-effective Friction Stir Welding Process for Use in Advanced Military Vehicles, *J. Mater. Eng. Perform.*, 2010. doi:10.1007/s11665-010-9650-0
30. M. Grujicic, G. Arakere, B. Pandurangan, A. Hariharan, C.-F. Yen, B.A. Cheeseman, and C. Fountzoulas, Computational Analysis and Experimental Validation of the Ti-6Al-4V Friction Stir Welding Behavior, *J. Eng. Manuf.*, April 2010, accepted
31. A. Cho and B. Bes, Damage Tolerance Capability of an Al-Cu-Mg-Ag Al2139 Aluminum Alloys, *Mater. Sci. Forum*, 2006, **519–521**, p 603–608
32. R.J. Chester and I.J. Polmear, "Precipitation in Al-Cu-Mg-Ag Alloys," *The Metallurgy of Light Alloys*, The Institution of Metallurgists, London, 1983, p 75–81
33. R.J. Chester and I.J. Polmear, TEM Investigation of Precipitates in Al-Cu-Mg-Ag and Al-Cu-Mg Alloys, *Micron*, 1980, **11**, p 311–312
34. I.J. Polmear and R.J. Chester, Abnormal Age Hardening in an Al-Cu-Mg Alloy Containing Silver and Lithium, *Scr. Metall.*, 1989, **23**, p 1213–1218
35. B.M. Gable, G.J. Shiflet et al., The Effect of Si Additions on Omega Precipitation in Al-Cu-Mg-(Ag) Alloys, *Scr. Mater.*, 2004, **50**, p 149–153
36. S.C. Wang and M.J. Starink, Precipitates and Intermetallic Phases in Precipitation Hardening Al-Cu-Mg-(Li) Based Alloys, *Int. Mater. Rev.*, 2005, **50**, p 193–215
37. L. Del Castillo and E.J. Lavernia, Microstructure and Mechanical Behavior of Spray-Deposited Al-Cu-Mg(-Ag-Mn) Alloys, *Metall. Mater. Trans. A Phys. Metall. Mater. Sci.*, 2000, **31**, p 2287–2298
38. K.M. Knowles and W.M. Stobbs, The Structure of (111) Age-Hardening Precipitates in Al-Cu-Mg-Ag Alloys, *Acta Crystallogr. B Struct. Sci.*, 1988, **44**, p 207–227
39. A.M. Zahra and C.Y. Zahra, Effects of Minor Additions of Mg and Ag on Precipitation Phenomena in Al-4 Mass% Cu, *Philos. Mag.*, 2004, **84**, p 2521–2541
40. O. Beffort, C. Solenthaler et al., Improvement of Strength and Fracture-Toughness of a Spray-Deposited Al-Cu-Mg-Ag-Mn-Ti-Zr Alloy by Optimized Heat-Treatments and Thermomechanical Treatments, *Mater. Sci. Eng. A Struct. Mater. Prop. Microstruct. Process.*, 1995, **191**, p 113–120
41. D. Vaughan, Grain Boundary Precipitation in an Al-Cu Alloy, *Acta Metall.*, 1968, **16**, p 563–577
42. W.M. Lee, Dynamic Microstructural Characterization of High Strength Aluminum Alloys, Master's Thesis, North Carolina State University, 2008
43. K. Hono, N. Sano et al., Atom Probe Study of the Precipitation Process in Al-Cu-Mg-Ag Alloys, *Acta Metall. Mater.*, 1993, **41**, p 829–838
44. S.P. Ringer and K. Hono, Microstructural Evolution and Age Hardening in Aluminium Alloys: Atom Probe Field-Ion Microscopy and Transmission Electron Microscopy Studies, *Mater. Charact.*, 2000, **44**, p 101–131
45. A. Garg, Y.C. Chang et al., Precipitation of the Omega-Phase in an Al-4.0Cu-0.5Mg Alloy, *Scr. Metall. Mater.*, 1990, **24**, p 677–680
46. ABAQUS Version 6.8-1, User Documentation, Dassault Systems, 2008
47. G.R. Johnson and W.H. Cook, "A Constitutive Model and Data for Metals Subjected to Large Strains, High Strain Rates and High Temperatures," *Proceedings of the 7th International Symposium on Ballistics*, 1983
48. L.E. Svensson, L. Karlsson, H. Larsson et al., Microstructure and Mechanical Properties of Friction Stir Welded Aluminium Alloys with Special Reference to AA 5083 and AA 6082, *Sci. Technol. Weld. Join.*, 2000, **5**, p 285–296
49. R.E. Reed-Hill, *Physical Metallurgy Principles*, PWS Publishing Company, MA, 1994

50. Y.S. Sato, M. Urata, H. Kokawa, and K. Ikeda, Hall-Petch Relationship in Friction Stir Welds of Equal Channel Angular-Pressed Aluminium Alloys, *Mater. Sci. Eng.*, 2003, **A354**, p 298–305
51. I. Charit and R.S. Mishra, Evaluation of Microstructure and Superplasticity in Friction Stir Processed 5083 Al Alloy, *J. Mater. Res.*, 2004, **19**, p 3329–3342
52. M. Grujicic, G. Arakere, B. Pandurangan, A. Hariharan, C.-F. Yen, B.A. Cheeseman and C. Fountzoulas, Statistical Analysis of High-Cycle Fatigue Behavior of Friction Stir Welded AA5083-H321, *J. Mater. Eng. Perform.*, 2010. doi:10.1007/s11665-010-9725-y
53. K. Kannan, J.S. Vetrano, and C.H. Hamilton, Effects of Alloy Modification and Thermomechanical Processing on Recrystallization of Al-Mg-Mn Alloys, *Metall. Mater. Trans.*, 1996, **27A**, p 2947–2957
54. M. Peel, A. Steuwer, M. Preuss, and P.J. Withers, Microstructure, Mechanical properties and Residual Stresses as a Function of Welding Speed in Aluminium AA5083 Friction Stir Welds, *Acta Mater.*, 2003, **51**, p 4791–4801
55. Y.S. Sato, S. Hwan, C. Park, and H. Kokawa, Microstructural Factors Governing Hardness in Friction-Stir Welds of Solid-Solution-Hardened Al Alloys, *Metall. Mater. Trans. A*, 2001, **32A**, p 3033–3042
56. D. Allehaux and F. Marie, Mechanical and Corrosion Behavior of the 2139 Aluminum-Copper-Alloy Welded by the Friction Stir Welding Using the Bobbin Tool Technique, *Mater. Sci. Forum*, 2006, **519–521**, p 1131–1138
57. L. Fratini, G. Buffa, and D. Palmeri, Using a Neural Network for Predicting the Average Grain-Size in Friction Stir Welding Processes, *Comput. Struct.*, 2009, **87**, p 1166–1174